PHYSICAL REVIEW A VOLUME 45, NUMBER 9 1 MAY 1992

Experimental and theoretical studies of the He^{2+}-He system: Differential cross sections for direct, single-, and double-charge-transfer scattering at keV energies

R. S. Gao, C. M. Dutta, N. F. Lane, K. A. Smith, and R. F. Stebbings
Physics Department, Rice University, P.O. Box 1892, Houston, Texas 77251;
Space Physics and Astronomy Department, Rice University, P.O. Box 1892, Houston, Texas 77251
and Rice Quantum Institute, Rice University, P.O. Box 1892, Houston, Texas 77251

M. Kimura
Argonne National Laboratory, Argonne, Illinois 60439
and Department of Physics, Rice University, Houston, Texas 77251
(Received 18 November 1991)

Measurements and calculations of differential cross sections for direct scattering, single charge transfer, and double charge transfer in collisions of 1.5-, 2.0-, 6.0-, and 10.0-keV $^3He^{2+}$ with a ^4He target are reported. The measurements cover laboratory scattering angles below 1.5° with an angular resolution of about 0.03°. A quantum-mechanical molecular-state representation is employed in the calculations; in the case of single charge transfer a two-state close-coupling calculation is carried out taking into account electron-translation effects. The theoretical calculations agree well with the experimental results for direct scattering and double charge transfer. For single charge transfer, the agreement is less satisfactory because of the limited number of molecular states incorporated in our calculations. The present calculation identifies the origins of oscillatory structures observed in the differential cross sections.

PACS number(s): 34.70.+e, 34.20.−b, 34.40.+n, 34.50.Lf

I. INTRODUCTION

The He^{2+}-He collision system has been the subject of several experimental and theoretical studies, and both total and differential cross sections for single- and double-charge-transfer scattering have been measured [1–3] and calculated [3–6] over a wide energy range. However, no measurements or calculations of differential angular scattering cross sections have previously been carried out for the He^{2+}-He collision system in the low-to-intermediate keV regime.

In this paper we report measurements and theoretical calculations of absolute differential cross sections for direct scattering (DS),

$$^3He^{2+}+{}^4He\rightarrow{}^3He^{2+}+{}^4He \tag{1}$$

at $^3He^{2+}$ energies of 1.5, 2.0, 6.0, and 10.0 keV, for double charge transfer (DCT),

$$^3He^{2+}+{}^4He\rightarrow{}^3He+{}^4He^{2+}\ , \tag{2}$$

at 2.0, 6.0, and 10.0 keV, and for single charge transfer (SCT),

$$^3He^{2+}+{}^4He\rightarrow{}^3He^{+}+{}^4He^{+}\ , \tag{3}$$

at 6.0 and 10.0 keV. The laboratory scattering angle range is between 0.03° and 1.5° with an angular resolution of 0.03° for DS and SCT, and between 0.02° and 1.5° with an angular resolution of 0.02° for DCT. Theoretical calculations are carried out using a fully quantum-mechanical molecular-orbital (MO) treatment of the collision system.

II. APPARATUS AND EXPERIMENTAL METHOD

Figure 1 shows a schematic of the apparatus. $^3He^{2+}$ ions emerging from the electron-impact ion source are accelerated to the desired beam energy and focused electrostatically. The resulting beam is momentum analyzed by a pair of 60° sector magnets and passes through a collimating aperture before arriving at the target cell (TC). The collimating aperture and the TC entrance aperture are 30 and 20 μm in diameter, respectively, and are separated by 19 cm, collimating the ion beam to less than 0.008° divergence. The TC is approximately 0.26 cm long and has an exit aperture 300 μm in diameter. A pair of deflection plates is placed immediately after the TC. A position-sensitive detector (PSD) that uses microchannel plates and a resistive anode is located 74 cm beyond the TC. A computer system (Motorola MVME 1131XT) monitors the output of the PSD electronics, sorting the arrival coordinates of each detected particle into bins in a square array. The physical bin size is $106\times106\ \mu m^2$, which is measured by observing the shadow of a nickel grid of known dimensions placed directly in front of the PSD as an ion beam is swept over its surface. This technique is also used to determine the position-finding accuracy of the PSD. Apparatus configurations for the experiments are as follows.

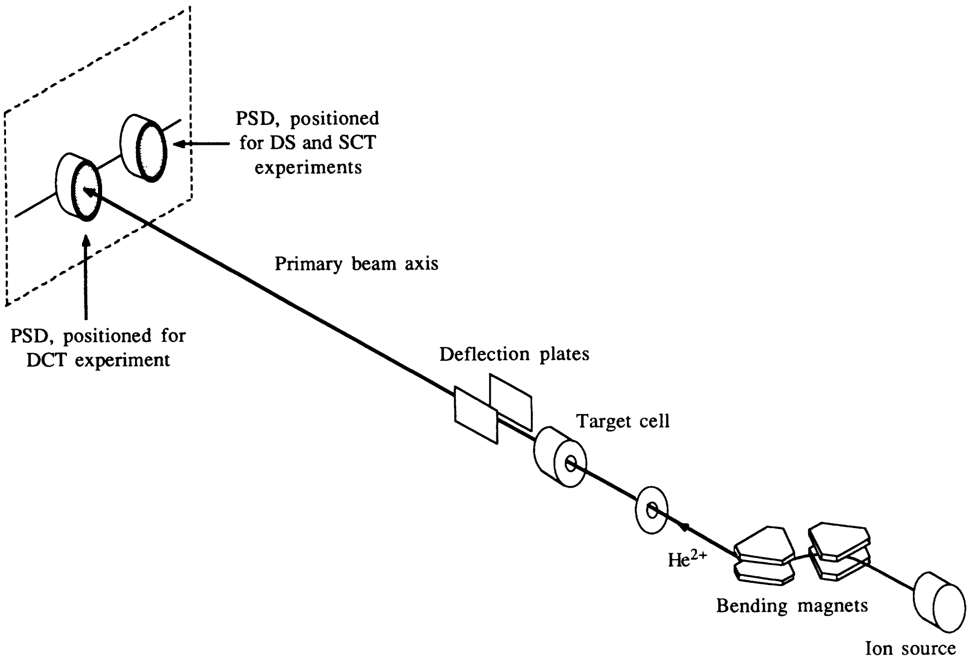

FIG. 1. Schematic of the apparatus.

A. Direct scattering experiment

As shown in Fig. 1, for the direct scattering experiment, the PSD's center is positioned 6.5 cm away from the primary beam axis, and the deflection plates are activated. In this configuration, the primary $^3He^{2+}$ beam and the directly scattered $^3He^{2+}$ are deflected to the PSD. The deflection plates were designed using SIMION [7], are biased symmetrically about ground, and have relatively large areas (8×8 cm^2) to reduce the focusing that accompanies deflection thereby minimizing distortions in the cylindrical symmetry of the deflected scattering pattern. The distortion introduced by these plates has been found to be negligible by deflecting He^+-He direct scattering products (which exhibit a very pronounced structure in their angular scattering), and measuring the resulting distortions in the cylindrical symmetry of the scattering pattern.

B. Double-charge-transfer-scattering experiment

The PSD is located on the primary beam axis. The deflection plates are used to deflect primary ions and charged scattering products away from the PSD so that only the neutral ^3He products of reaction (2) are detected. The primary ion flux is measured intermittently during the neutral-particle measurement by removing the deflection field.

C. Single-charge-transfer-scattering experiment

The apparatus configuration is the same as for the direct scattering experiment, except that the deflection field is now adjusted so that the singly charged scattering products impact the PSD. The primary beam intensity is intermittently monitored by the PSD in this experiment also.

Under the thin target conditions used in this experiment, the differential cross sections are determined from the measured quantities by the expression

$$\frac{d\sigma(\theta)}{d\Omega}=\frac{\Delta S(\theta)}{SnL\Delta\Omega}, \tag{4}$$

where S is the primary ion beam flux in particles per second, $\Delta S(\theta)$ is the flux of the product particles scattered between angles $\theta-\Delta\theta/2$ and $\theta+\Delta\theta/2$ into a solid angle $\Delta\Omega$ sr, n is the target number density obtained from a measurement of gas pressure in the TC, and L is the physical length of the target cell. A typical target cell pressure is 5 mTorr, resulting in a residual vacuum chamber pressure of below 2×10^{-7} Torr. Under these conditions, less than 1% of the beam is scattered by the target gas. Two square data arrays, one with gas in the target cell and one without, are taken for every reaction. The scattered flux, $\Delta S(\theta)$, is obtained by organizing the arrays into concentric rings and subtracting the gas-out data from the gas-in data. This procedure permits removal of the primary ion beam signal in the case of direct scattering, and allows discrimination between counts due to scattering from the target gas and counts arising from other sources, such as PSD dark counts or scattering from the background gas and edges of apertures.

The issue of relative detection efficiencies for neutral and charged species has been discussed previously [8,9] with the conclusion that above 5.0 keV, the two efficiencies are considered equal for the detector used in this experiment. At 2.0 keV, however, there is possibly a difference of a few percent. The experimental uncertainty in the number of counts at a particular angle is primarily statistical. The angular uncertainty arises from the finite width of the primary ion beam, the discrete width of the analysis rings, and electronic errors in the detector's position encoding circuits.

III. THEORETICAL CONSIDERATIONS

The theoretical approach used here is the same as that successfully applied earlier in a calculation of charge-transfer cross sections for the H^+-He system [10]. Therefore we will not repeat the details. The relevant adiabatic potentials of the He_2^{2+} molecule are shown in Fig. 2. In calculating differential cross sections for the DS and DCT processes, we included only the $2\,{}^1\Sigma_g$ and $1\,{}^1\Sigma_u$ adiabatic potentials. Other ${}^1\Sigma_u$ states are energetically remote, and weakly coupled except in the very-small-internuclear-distance (R) region. For the g symmetry, an avoided crossing at $R \sim 1.4$ a.u. with the next higher g state, as well as avoided crossings among other higher g states, may be viewed as resulting in a diabatic state that correlates with the σ_u^2 MO pairs in the united-atom limit [11]. We will denote this diabatic state $2\,{}^1\Sigma_g^d$. We examine later the sensitivity of the DS and DCT differential cross sections to the choice of the adiabatic $2\,{}^1\Sigma_g$ or diabatic $2\,{}^1\Sigma_g^d$ energy curve at various scattering angles. Because of the difference in electronic symmetry, the ${}^1\Sigma_g$ and ${}^1\Sigma_u$ states are dynamically uncoupled so that double charge transfer occurs only due to interference between the gerade and ungerade scattering amplitudes, since the two states are asymptotically degenerate (resonance charge transfer). The differential cross sections are given for direct scattering by the expression

$$\frac{d\sigma(\theta)}{d\Omega}=\frac{1}{4k^2}\left[\sum_l (2l+1)(1-S_{\mathrm{DS}}^l)P_l(\cos\theta)\right]^2 , \qquad (5)$$

where

$$S_{\mathrm{DS}}^l=\frac{S_g^l+S_u^l}{2} , \qquad (6)$$

and for double charge transfer by

$$\frac{d\sigma(\theta)}{d\Omega}=\frac{1}{4k^2}\left[\sum_l (2l+1)S_{\mathrm{DCT}}^l P_l(\cos\theta)\right]^2 , \qquad (7)$$

where

$$S_{\mathrm{DCT}}^l=\frac{S_g^l-S_u^l}{2} . \qquad (8)$$

In Eqs. (6) and (8), S_g^l and S_u^l are the (diagonal) S-matrix elements corresponding to lth partial wave for the $2\,{}^1\Sigma_g$ (or ${}^1\Sigma_g^d$) and $1\,{}^1\Sigma_u$ states, respectively. This approach explicitly neglects the single-charge-transfer channel. It is justifiable at small angles because the cross section for SCT is much smaller than those for DCT and DS.

In the calculation of the SCT differential cross sections, we assume that at the low energies of present interest the final states are dominated by the $He^+(1s)$-$He^+(n=2)$ manifold, which involves the molecular states $1\,{}^1\Sigma_u$, $2\,{}^1\Sigma_u$, $1\,{}^1\Pi_u$, and $2\,{}^1\Sigma_g$, $3\,{}^1\Sigma_g$, $1\,{}^1\Pi_g$. In Fig. 3 we show the radial coupling matrices among the Σ states. For both the gerade-gerade and ungerade-ungerade cases, the angular couplings are weak; and hence we ignore two small contributions from the Π states. Indeed, three-state (two Σ's and one Π) calculations verify this assumption. For the sake of computational convenience, the coupled equations are simplified by the "diabatic transformation" [12,13], and the resulting scattering equations are

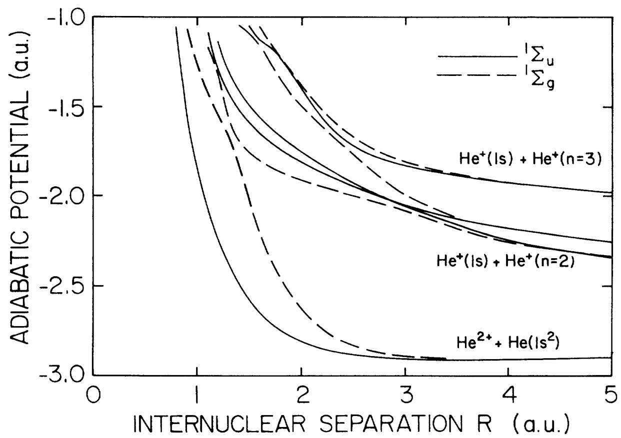

FIG. 2. Adiabatic potentials for singlet He_2^{2+} system. The lowest $1\,{}^1\Sigma_g$ state is not shown. The solid lines are $1\,{}^1\Sigma_u$, $2\,{}^1\Sigma_u$, $3\,{}^1\Sigma_u$, and $4\,{}^1\Sigma_u$, and the dashed lines are $2\,{}^1\Sigma_g$, $3\,{}^1\Sigma_g$, $4\,{}^1\Sigma_g$, and $5\,{}^1\Sigma_g$.

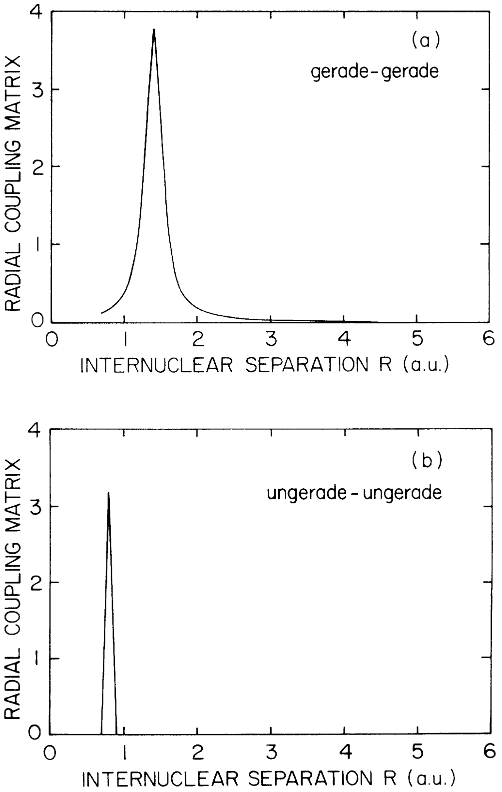

FIG. 3. (a) Radial coupling matrices between the gerade states $2\,{}^1\Sigma_g$ and $3\,{}^1\Sigma_g$. (b) Radial coupling matrices between the ungerade states $1\,{}^1\Sigma_u$ and $2\,{}^1\Sigma_u$.

solved by the log-derivative method [14]. In the transformation, the C-matrix [13] is obtained by fitting the radial coupling matrices by Lorentzian-type functions. We also point out that the molecular orbitals used here are less accurate at very small R because of the limited choice of basis sets, and we choose the minimum R value to be 0.7 a.u. instead of zero.

IV. RESULTS AND DISCUSSION

A. Differential cross sections for the DS and DCT processes

Cross sections for DS and DCT have been calculated using two different choices for the potential energy functions: (a) the adiabatic $2\,^1\Sigma_g$ and $1\,^1\Sigma_u$ potentials shown in Fig. 2, and (b) a diabatic potential $2\,^1\Sigma_g^d$ constructed by smoothly combining segments of the adiabatic potentials corresponding to $2\,^1\Sigma_g$, $3\,^1\Sigma_g$, $4\,^1\Sigma_g$, $5\,^1\Sigma_g$, and $6\,^1\Sigma_g$, while keeping the potential for $1\,^1\Sigma_u$ adiabatic. In Fig. 4, the adiabatic and diabatic potentials are plotted. Calculated cross sections, differential with respect to laboratory scattering angle θ, are shown in Figs. 5–8. We observe that agreement between the calculated and experimental DS and DCT cross sections is generally good below a reduced scattering angle (product of the collision energy and scattering angle) of about 1 keV deg for both choices of the potentials. This result is not unexpected, since the contributions to the cross sections at small angles come from large impact parameters, and hence from large values of R, where both sets of potentials are nearly identical. However, at higher energies and larger angles (reduced scattering angles ~ 7 keV deg), the angular distributions corresponding to the different potentials vary considerably, and the differences increase with increasing reduced scattering angle. At these reduced scattering angles, the adiabatic potential $2\,^1\Sigma_g$ yields rather poor agreement with experiment, while the diabatic potential $2\,^1\Sigma_g^d$ adequately describes the observed scattering up to about 1 keV deg. Both choices of potentials fail to describe the observed scattering adequately at reduced scattering angles greater than 7 keV deg. This is not surprising because the coupling to the other states can no longer be ignored in these hard collisions; in fact, the differential cross sections for SCT become comparable to that for DS and DCT, and therefore the simple two-potential calculations we used for DS and DCT are not adequate.

In Fig. 9 we show the dependence, on l, of the squared absolute value of the relevant DCT S-matrix element S^l_{DCT} defined in Eq. (8) at $E=2.0$ keV for the adiabatic potentials $2\,^1\Sigma_g$ and $1\,^1\Sigma_u$. Associating these with the classical deflection angles computed from the phase of the S matrix [15], we can then correlate the structure in the differential cross sections with features of the potential. In this example, contributions to the broad maxima in the DCT cross section of Fig. 6(b) at $0.2° \le \theta \le 0.5°$ (the impact parameter $b \sim 1.95$ a.u.) and $\theta \sim 1°$ ($b \sim 1.40$ a.u.) arise from the peaks A and B in Fig. 9, respectively; and the valley at $\theta \sim 0.87°$ arises from the minimum C around $l \sim 820$ ($b \sim 1.56$ a.u.). Angles corresponding to other peaks and valleys are outside the angular range of measurement. Similar analyses for DCT and DS over a range of energies probe different regions of the potentials.

The differential cross sections are rich in structure, exhibiting many undulations. The relatively sharp alternative maxima and minima in the DS and DCT cross sections are due to interference between the gerade and ungerade scattering amplitudes. At smaller angles (e.g., $\theta \le 0.2°$ at 2.0 keV), diffraction effects caused by interfer-

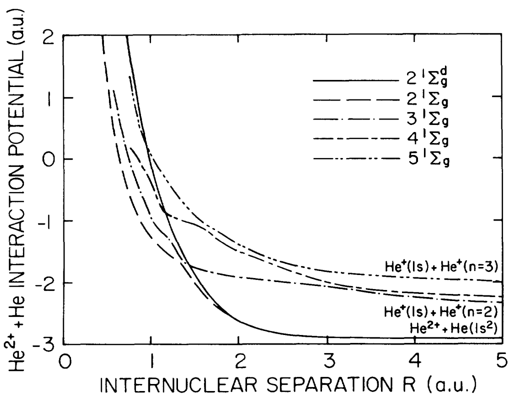

FIG. 4. Comparisons of the adiabatic $2\,^1\Sigma_g$, $3\,^1\Sigma_g$, $4\,^1\Sigma_g$, $5\,^1\Sigma_g$, and the diabatic $2\,^1\Sigma_g^d$ potentials.

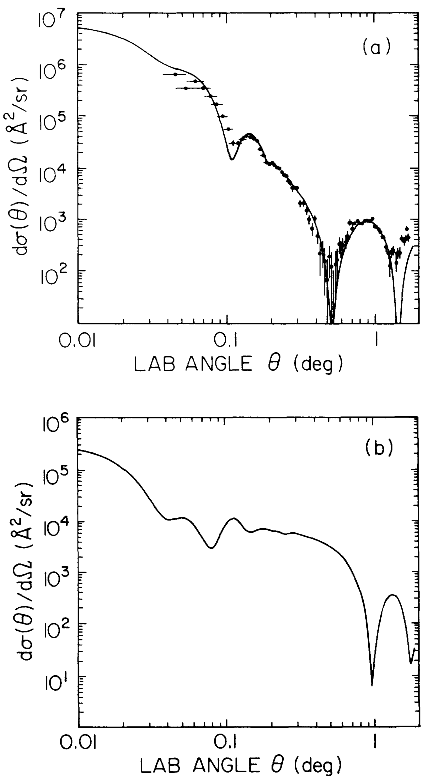

FIG. 5. (a) Differential cross sections for DS at 1.5 keV. + + + +, experimental results with error bars; ——, calculated from the diabatic potentials. (b) Differential cross sections for DCT at 1.5 keV, calculated from the diabatic potentials.

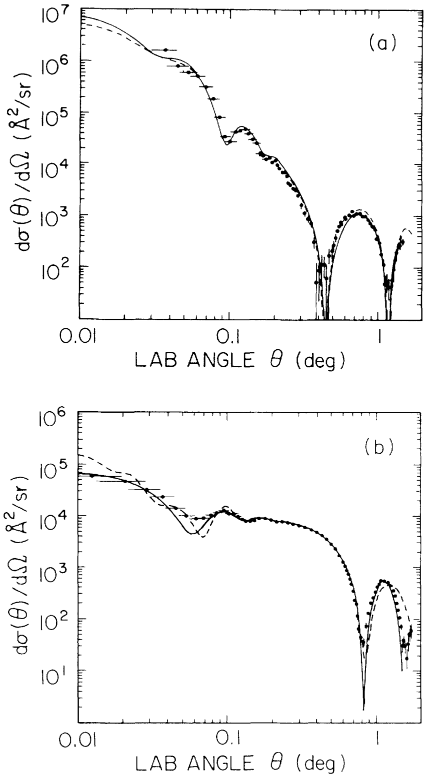

FIG. 6. (a) Differential cross sections for DS at 2.0 keV. + + + +, experimental results with error bars; ——, calculated from the diabatic potentials; and — — —, calculated from adiabatic potentials. (b) Differential cross sections for DCT at 2.0 keV. + + + +, experimental results with error bars; ——, calculated from the diabatic potentials; and — — —, calculated from adiabatic potentials.

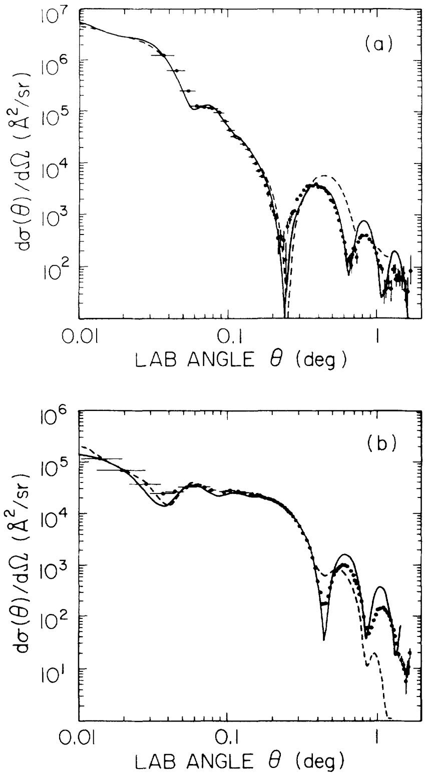

FIG. 7. (a) Differential cross sections for DS at 6.0 keV. + + + +, experimental results with error bars; ——, calculated from the diabatic potentials; and — — —, calculated from adiabatic potentials. (b) Differential cross sections for DCT at 6.0 keV. + + + +, experimental results with error bars; ——, calculated from the diabatic potentials; and — — —, calculated from adiabatic potentials.

ence of many l waves from the single gerade or ungerade potential are observed as well. These diffraction peaks can be identified computationally by eliminating the interference terms between S_g^l and S_u^l in calculating the $|1-S_{\rm DS}^l|^2$ and $|S_{\rm DCT}^l|^2$ terms in Eqs. (5) and (7). At 1.5 keV, for example, the small peaks in the DS cross sections at $\theta \leq 0.2^\circ$ are diffraction peaks [8,10,16,17] arising from the steep repulsive walls of the potentials. The feature at $\theta \sim 0.04^\circ$ is due to rainbow scattering, which is caused by interference between two classical trajectories that correspond to the same scattering angle but that carry a different scattering phase [15]; this effect is due to the presence of the shallow attractive well in the u potential.

B. Differential cross sections for SCT processes

We assume, as stated earlier, that at the energies studied here, the SCT process is dominated by g-g and u-u radial coupling at the avoided crossings between the most strongly coupled $^1\Sigma_g$ and $^1\Sigma_u$ states (see Fig. 3). The peaks in the radial coupling matrix elements are seen in Figs. 3(a) and 3(b) to be at 1.4 a.u. for the gerade and 0.8 a.u. for the ungerade states, and in our calculations, most transitions occur near these R values. Computed differential cross sections are shown in Figs. 10 and 11, together with the experimental results. The overall angular dependence of the experimental SCT cross sections is reproduced by the present calculation. However, the quantitative agreement is less satisfactory, especially at very small and large scattering angles. At smaller R, where most of the single charge transfer occurs in the present case, there are many higher-lying states which we do not include but which could be important. We conclude that the present two-state description is not good enough to give quantitative agreement at energies as high as 10 keV. At these relatively high energies, classical turning points for small-l partial waves are less than the minimum value $R = 0.7$ a.u. used in the calculations. This cutoff at small R may be responsible for the rapid oscillations in the computed differential cross sections at large scattering angles.

V. SUMMARY

We have presented a fairly complete picture of He^{2+}-He collisions in the keV energy range, comprising both

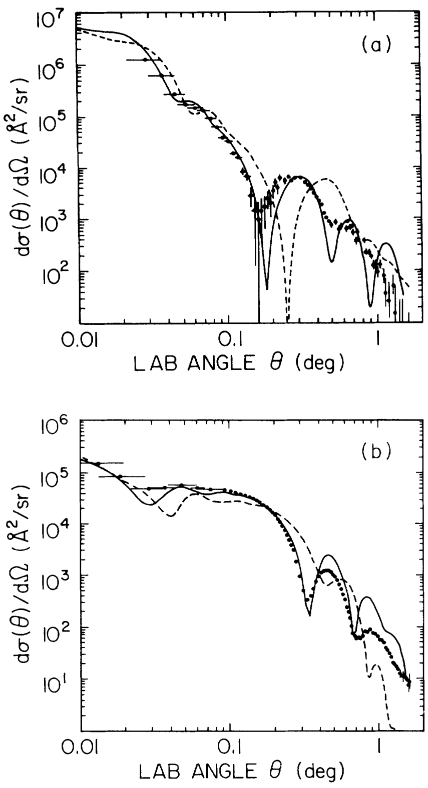

FIG. 8. (a) Differential cross sections for DS at 10.0 keV. + + + +, experimental results with error bars; ——, calculated from the diabatic potentials; and — — —, calculated from adiabatic potentials. (b) Differential cross sections for DCT at 10.0 keV. + + + +, experimental results with error bars; ——, calculated from the diabatic potentials; and — — —, calculated from adiabatic potentials.

experimental and theoretical studies. A two-potential treatment of differential cross sections for DS and DCT in He^{2+}-He collisions at laboratory energies below 10 keV and scattering angles below 1° gives satisfactory agreement with the measurements, provided that a diabatic $^1\Sigma_g$ state is properly constructed. In the case of SCT, where the dominant mechanism is nonadiabatic coupling, only a few ($^1\Sigma_g$ and $^1\Sigma_u$) states need be included in the close-coupling expansion for reasonably good qualitative agreement at these energies. The present calculation successfully gives a theoretical rationale to oscillatory structures observed in terms of impact parameters and scattering angles. At larger scattering angles, and higher energies, agreement between the SCT theory and experiment is less satisfactory, indicating that the diabatic potential in the small internuclear separation may require further improvement. In addition, inclusion of other channels may be necessary for the correct description of SCT at larger scattering angles and higher collision energies.

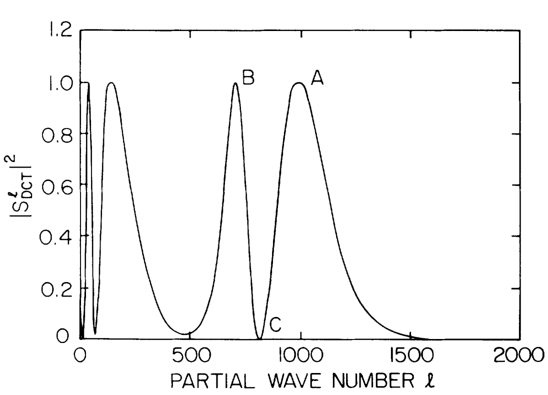

FIG. 9. $|S^{l}_{DCT}|^2$ vs l at 2.0 keV, using the adiabatic potentials.

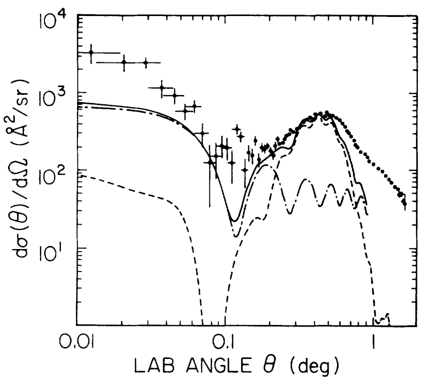

FIG. 10. Differential cross sections for SCT at 6.0 keV. + + + +, experimental results with error bars; ——, calculation; — — —, contribution from gerade-gerade transition; —·—·—·, contribution from ungerade-ungerade transition.

ACKNOWLEDGMENTS

The experimental work was supported by the Robert A. Welch Foundation, NASA, and the NSF Atmospheric

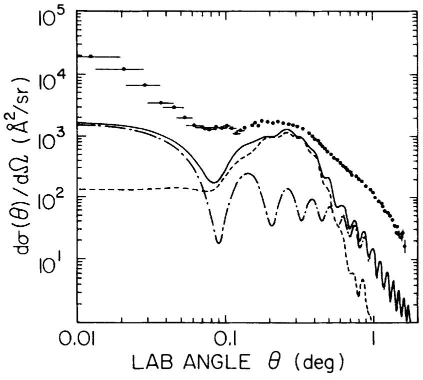

FIG. 11. Differential cross sections for SCT at 10.0 keV. + + + +, experimental results with error bars; ——, calculation; — — —, contribution from gerade-gerade transition; —·—·—·, contribution from ungerade-ungerade transition.

Sciences Section. In the theoretical work, M. Kimura has been supported in part by the U.S. Department of Energy, Assistant Secretary of Energy Research, Office of Health and Environmental Research, under Contract No. W-31-109-Eng-38, and C. M. Dutta and N. F. Lane were supported in part by the U.S. Department of Energy, Office of Basic Energy Sciences, Division of Chemical Sciences, and the Robert A. Welch Foundation.

[1] J. E. Bayfield and G. A. Khayrallah, Phys. Rev. A **11**, 920 (1975).
[2] V. V. Afrosimov, A. A. Basalen, G. A. Leiko, and M. N. Panov, Zh. Eksp. Teor. Fiz. **74**, 1605 (1978) [Sov. Phys. JETP **47**, 837 (1978)].
[3] S. K. Lam, L. D. Doverspike, and R. L. Champion, Phys. Rev. A **71**, 595 (1973).
[4] C. Harel and A. Salin, J. Phys. B **13**, 785 (1980).
[5] K. R. S. Devi and J. D. Garcia, J. Phys. B **16**, 2837 (1983).
[6] M. Kimura, J. Phys. B **21**, L19 (1988).
[7] For more information about program SIMION, contact Dr. D. A. Dahl, MS 2208, EG&G Idaho Inc., Idaho National Engineering Laboratory, P. O. Box 1625, Idaho Falls, ID 83415.
[8] R. S. Gao, L. K. Johnson, D.A. Schafer, J. H. Newman, K. A. Smith, and R. F. Stebbings, Phys. Rev. A **38**, 2789 (1988).
[9] R. S. Gao, P. S. Gibner, J. H. Newman, K. A. Smith, and R. F. Stebbings, Rev. Sci. Instrum. **55**, 1756 (1984).
[10] L. K. Johnson, R. S. Gao, R. A. Dixson, K. A. Smith, N. F. Lane, R. F. Stebbings, and M. Kimura, Phys. Rev. A **40**, 3626 (1989).
[11] *Electronic and Ionic Impact Phenomena,* edited by H. S. W. Massey, E. H. S. Burhop, and H. B. Gilbody (Oxford University, New York, 1969), Vol. IV, p. 2546.
[12] J. B. Delos and W. R. Thorson, Phys. Rev. A **18**, 117 (1978).
[13] T. G. Heil, S. E. Butler, and A. Dalgarno, Phys. Rev. A **23**, 1100 (1981).
[14] B. R. Johnson, J. Comput. Phys. **13**, 445 (1973).
[15] K. W. Ford and J. A. Wheeler, Ann. Phys. (N.Y.) **7**, 259 (1959).
[16] R. P. Marchi and F. T. Smith, Phys. Rev. A **139**, 1025 (1965).
[17] R. S. Gao, L. K. Johnson, D. E. Nitz, K. A. Smith, and R. F. Stebbings, Phys. Rev. A **36**, 3077 (1987).

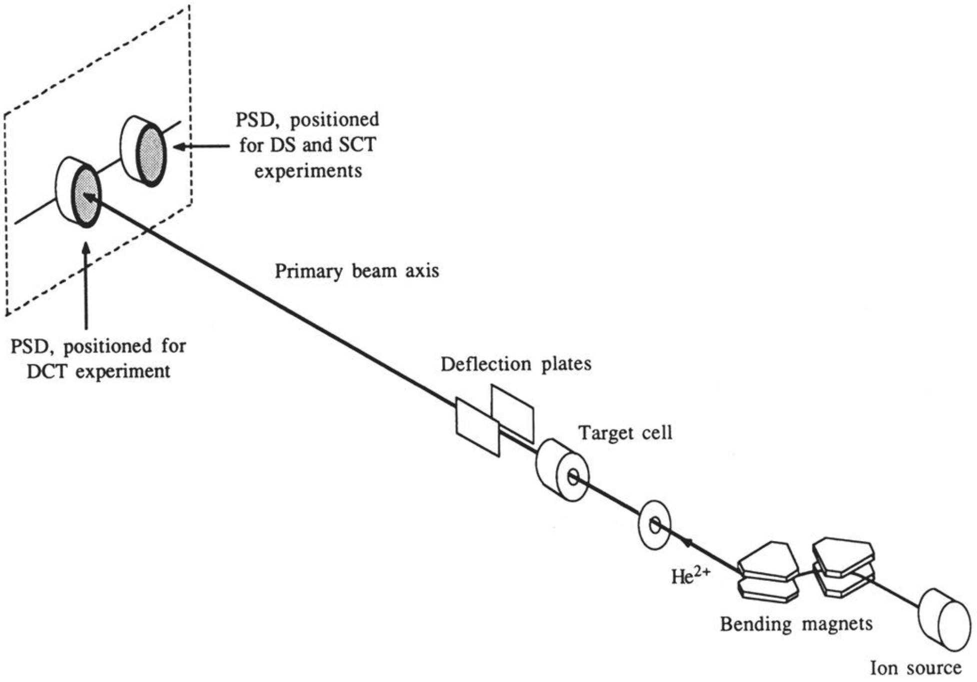

FIG. 1. Schematic of the apparatus.